Journal of Instrumentation

PAPER • **OPEN ACCESS**

Performance in beam tests of irradiated Low Gain Avalanche Detectors for the ATLAS High Granularity Timing Detector

To cite this article: C. Agapopoulou *et al* 2022 *JINST* **17** P09026

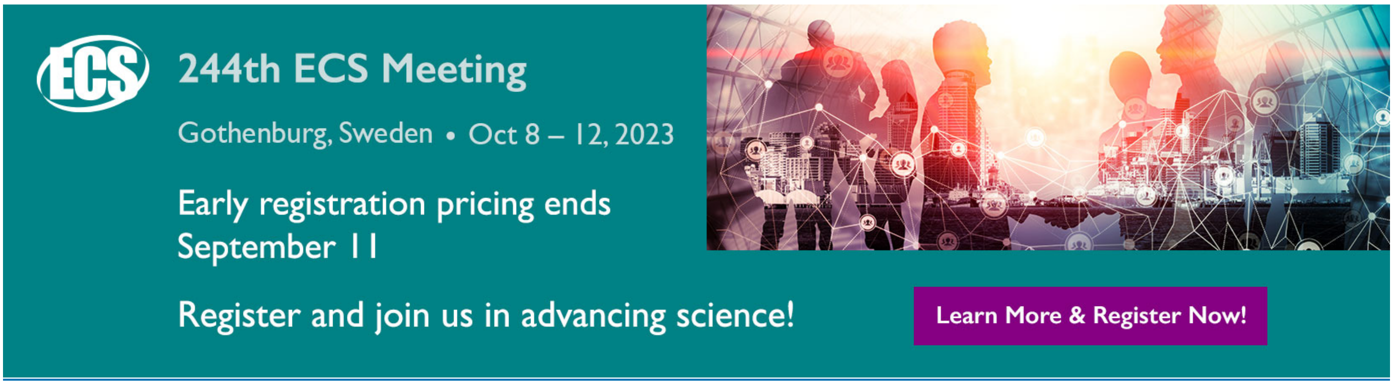

Published by IOP Publishing for Sissa Medialab

Received: *June 29, 2022*
Accepted: *August 6, 2022*
Published: *September 21, 2022*

Performance in beam tests of irradiated Low Gain Avalanche Detectors for the ATLAS High Granularity Timing Detector

2022 JINST 17 P09026

C. Agapopoulou,[a] S. Alderweireldt,[b] S. Ali,[c] M.K. Ayoub,[d] D. Benchekroun,[e] L. Castillo García,[f,*] Y.H. Chan,[g] H. El Jarrari,[c,h] A. Falou,[a] A. Ferreira,[b] E.L. Gkougkousis,[f] C. Grieco,[f] S. Grinstein,[f,i] J. Große-Knetter,[j] J. Guimarães da Costa,[d] S. Guindon,[b] A.M. Henriques Correia,[b] S. Hidalgo,[k] A. Howard,[l] P.J. Hsu,[g] Y.C. Huang,[g] Y. Khoulaki,[e] G. Kramberger,[l] E.S. Kuwertz,[b] J. Lange,[j] C. Li,[m] Q. Li,[m] H.C. Lin,[g] Y.J. Lu,[g] N. Makovec,[a] L. Masetti,[n] R. Mazini,[c] S.M. Mazza,[o] I. Nikolic,[p] G. Pellegrini,[k] A. Quadt,[j] B. Reynolds,[q] C. Rizzi,[b] M. Robles Manzano,[n] A. Rummler,[b] S. Sacerdoti,[a] L. Serin,[a] J. Soengen,[n] Y. Tayalati,[h] S. Terzo,[f] E. Tolley,[q] S. Trincaz-Duvoid,[p] S.M. Wang[c] and X. Yang[m]

[a] *Laboratoire de Physique des 2 Infinis Irène Joliot Curie (IJCLab),*
15 Rue Georges Clemenceau, 91400 Orsay, France

[b] *Conseil Européen pour la Recherche Nucléaire (CERN),*
Esplanade des Particules 1, CH-1211 Meyrin, Switzerland

[c] *Academia Sinica, 128, section 2, Academia Road, Nangang District, Taipei City 115, Taiwan*

[d] *Institute of High Energy Physics (IHEP), 19 Yuquan Road, Shijingshan District, Beijing, China*

[e] *Université Hassan II, Casablanca 20000, Morocco*

[f] *Institut de Física d'Altes Energies (IFAE), The Barcelona Institute of Science and Technology (BIST),*
Carrer Can Magrans s/n, Edifici Cn, Campus UAB, E-08193 Bellaterra (Barcelona), Spain

[g] *National Tsing Hua University (NTHU), 101 Section 2,*
Kuang-Fu Road, East District, Hsinchu 300044, Taiwan

[h] *Université Mohammed V de Rabat, Avenue des Nations Unies, Agdal, Rabat, Morocco*

[i] *Institució Catalana de Recerca i Estudis Avançats (ICREA),*
Passeig de Lluís Companys, 23, 08010 Barcelona, Spain

[j] *Physikalisches Institut, Georg-August-Universität, Friedrich-Hund-Platz 1, D-37077 Göttingen, Germany*

[k] *Centro Nacional de Microelectrónica (CNM), Campus UAB, E-08193 Bellaterra (Barcelona), Spain*

[l] *Jožef Stefan Institute (JSI), Jamova cesta 39, 1000 Ljubljana, Slovenia*

[m] *Department of Modern Physics and State Key Laboratory of Particle Detection and Electronics,*
University of Science and Technology of China (USTC),
96 JinZhai Road Baohe District, Hefei, Anhui, 230026, China

[n] *Johannes Gutenberg Universität Mainz, Saarstraße 21, 55122 Mainz, Germany*

---

[*] Corresponding author.

https://doi.org/10.1088/1748-0221/17/09/P09026

[o] *Santa Cruz Institute for Particle Physics (SCIPP), University of California Santa Cruz,*
1156 High Street, Santa Cruz, CA 95064, U.S.A.
[p] *Laboratoire de Physique Nucléaire et de Hautes Energies (LPNHE), Sorbonne Université,*
Université de Paris, CNRS/IN2P3, Paris, France
[q] *Ohio State University, 281 W Lane Ave, Columbus, OH 43210, U.S.A.*

E-mail: `lucia.castillo.garcia@cern.ch`

Abstract: The High Granularity Timing Detector (HGTD) will be installed in the ATLAS detector to mitigate pile-up effects during the High Luminosity (HL) upgrade of the Large Hadron Collider (LHC) at CERN. The design of the HGTD is based on the use of Low Gain Avalanche Detectors (LGADs), with an active thickness of 50 µm, that allow to measure with high-precision the time of arrival of particles. The HGTD will improve the particle-vertex assignment by measuring the track time with a resolution ranging from approximately 30 ps at the beginning of the HL-LHC operations to 50 ps at the end. Performances of several unirradiated, as well as neutron- and proton-irradiated, LGAD sensors from different vendors have been measured in beam test campaigns during the years 2018 and 2019 at CERN SPS and DESY. This paper presents the results obtained with data recorded by an oscilloscope synchronized with a beam telescope which provides particle position information within a resolution of a few µm. Collected charge, time resolution and hit efficiency are presented. In addition to these properties, the charge uniformity is also studied as a function of the position of the incident particle inside the sensor pad.

Keywords: Si microstrip and pad detectors; Timing detectors

Contents

1 Introduction

The High Luminosity upgrade of the Large Hadron Collider (HL-LHC) [1, 2] at CERN is expected to deliver an integrated luminosity of 4000 fb^{-1} with an in increase of the instantaneous luminosity from $10^{34}\,\text{cm}^{-2}s^{-1}$ to $7.5 \times 10^{34}\,\text{cm}^{-2}s^{-1}$ resulting in a nominal average of 200 simultaneous pp interactions per bunch crossing. The correct assignment of particles originating from the hard-scattering process and the suppression of detector signals produced by the additional low-energy pp collisions (pile-up) are among the most difficult challenges in this busy environment.

A High Granularity Timing Detector (HGTD) [3, 4] installed at the end-cap/forward region of the ATLAS detector [5] with a pseudorapidity, η, coverage of 2.4 to 4.0 would provide additional capabilities to the foreseen new inner tracker [6, 7] to mitigate pile-up effects on physics final states containing forward jets/particles. Due to the high radiation levels expected in this region for an integrated luminosity of $4000\,\mathrm{fb}^{-1}$, the detector sensors and front-end electronics must sustain a 1 MeV neutron equivalent fluence of up to $2.5 \times 10^{15}\,\mathrm{n_{eq}/cm^2}$ and 2 MGy of total ionising dose estimated at a distance of 120 mm from the beam pipe. Assuming a safety factor of 1.5, the inner (middle) ring of the detector should be replaced at every $1000\,\mathrm{fb}^{-1}$ ($2000\,\mathrm{fb}^{-1}$) in order to keep its performances at an optimal level. The HGTD would be able to measure the time of a minimum ionising particle (MIP) with a resolution ranging from approximately 30 ps at the beginning of the HL-LHC operations to 50 ps towards the end, with an average time resolution per hit of 35 ps and 70 ps, respectively. Given the need for an accurate time measurement and a high radiation hardness, the Low Gain Avalanche Detector (LGAD) technology [8] was chosen for the sensors with an active thickness of 50 µm and a pad area of $1.3 \times 1.3\,\mathrm{mm}^2$. The time resolution is strongly linked to the front-end analog performance, which makes the read-out ASIC a very challenging circuit to design. The time jitter should be low enough to not deteriorate the sensor performance. The HGTD ASIC, ATLAS LGAD Time Read Out Chip (ALTIROC) [9], has a discriminator of ~ 2 fC and should achieve a good time measurement for charges as low as 4 fC, to cope with the reduction of the sensor gain due to irradiation. This lower limit on charge collection of 4 fC should satisfy the HGTD requirements of a minimum hit efficiency of 95% taking into account the ALTIROC jitter. The final ALTIROC is under design, where early prototypes are being tested at both laboratory and beam lines to validate their performances and readiness for the HL-LHC requirements [4, 10].

This paper presents the performance of LGAD sensors, mounted on custom electronic boards, using the data collected in 2018 and 2019. In 2018 the tests were carried out at the CERN SPS [11] with a high-energy pion beam, while in 2019 they were carried out at the DESY II Test Beam Facility [12] with an electron beam. Previous results for unirradiated and irradiated LGADs and first HGTD hybrid modules can be found in refs. [10, 13, 14]. This paper is organised as follows: in section 2 the LGAD technology and the tested sensors are described, while the test beam set-up and the data acquisition system are presented in section 3. The data processing and the analysis methods are detailed in section 4, followed by the presentation and discussion of the results in section 5. The conclusions are presented in section 6.

2 Sensors

This section describes the main features and properties of the tested sensors. Several irradiation campaigns were carried out and the different irradiation levels are indicated. The initial electrical characterization is also presented.

2.1 Low Gain Avalanche Detectors

The LGAD sensors are thin n-on-p silicon devices whose design [8, 15] has been originally developed by the Centro National de Microelectrónica (CNM) Barcelona within the CERN-RD50 collaboration [16]. Their geometry was later optimized for high-precision time measurements.

LGADs are based on implanting a few micrometer-thick, highly doped p-type layer between the high-resistivity p-type bulk and the n^+ implant (figure 1), which acts as a high-field charge multiplication layer providing a moderate gain of about 5 to 70.

The tested prototypes have been manufactured by CNM and Hamamatsu Photonics (HPK). Wafers (W) from both vendors contain a variety of pad structures, such as single-pad diodes and segmented arrays of pad diodes with various granularities. CNM sensors were produced on 4-inch silicon-on-silicon wafers with an active thickness of 50 µm and a resistivity of 12 kΩ cm on a 300 µm-thick support wafer and 1 µm buried oxide (see figure 1). In order to improve the radiation hardness, CNM investigated different doping materials: Boron for wafer 4,[1] Boron plus Carbon for wafer 5[1] and Gallium for wafer 6[2] [17]. Carbon-enriched LGADs aimed to obtain similar performances as Boron ones but at a lower bias voltages. On the other hand, HPK sensors were produced on 6-inch silicon-on-insulator wafers with an active thickness of 45 µm and a resistivity of 3.4 kΩ cm to 4.6 kΩ cm. HPK used only Boron to manufacture two types of LGADs with different doping profiles, a gain layer depth of 1.6 µm for the type-3.1 and 2.2 µm for the type-3.2, edge sizes of 300 µm and 500 µm as well as different nominal inter-pad distances (from 30 µm to 95 µm) in the case of 2×2 arrays. The tests reported in this paper were performed on CNM single-pad sensors with an overall active area of $1 \times 1\,\text{mm}^2$ and a gain layer of about $0.7 \times 0.7\,\text{mm}^2$ with a single guard ring (GR) structure of 0.135 mm and on HPK single-pad and 2×2 array sensors with an overall active area of $1.3 \times 1.3\,\text{mm}^2$. Figure 2 shows a schematic view of the CNM and HPK single-pad LGAD sensors.

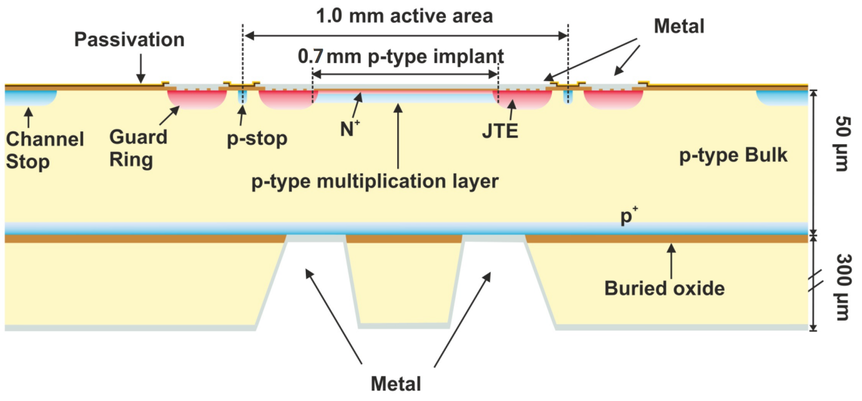

Figure 1. Cross section of a single-pad CNM LGAD sensor.

2.2 Irradiation

Radiation damage in silicon mainly results in the reduction of the effective doping concentration and the acceptor removal, by introducing trapping centers that reduce the mean free path of the charge carrier and increasing the leakage current [16]. A surface effect is the accumulation of positive charge in the oxide (SiO_2) and the Si-SiO_2 interface which affects the interpixel capacitance. This clearly has

---

[1] CNM production run 10478.

[2] CNM production run 10924.

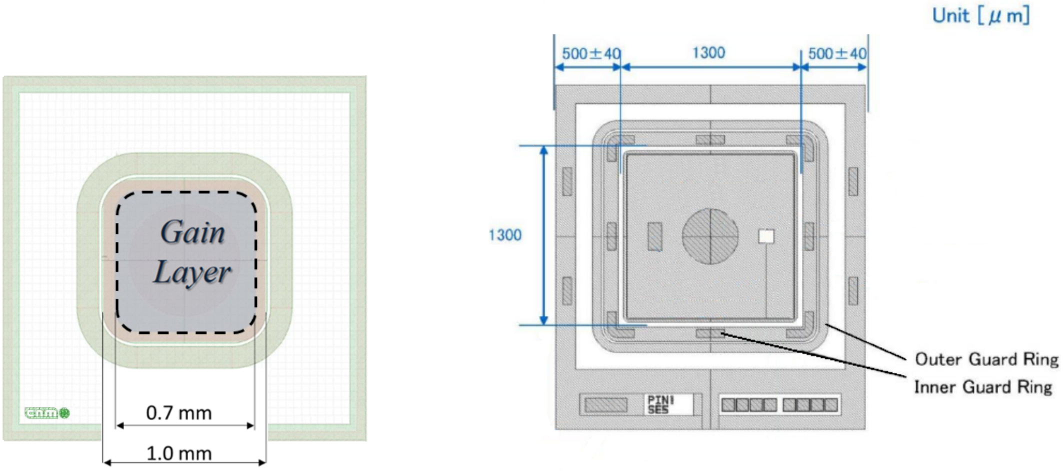

Figure 2. Geometry of CNM (left) and HPK 3.1 (right) single-pad LGAD sensors.

an impact on the detector performance and the charge collection efficiency. For LGADs, the radiation damage results in the degradation of the gain with fluence at a fixed voltage [18], which implies the need to increase the applied bias voltage after irradiation to at least partially compensate for this loss.

In order to study the LGAD performance after irradiation, the sensors were exposed to fluences up to $3 \times 10^{15}\ \mathrm{n_{eq}}/cm^2$ at various facilities with different particle types and energies. The main facilities are the TRIGA reactor in Ljubljana for 1 MeV neutrons, the CERN Proton Synchrotron (PS) IRRAD facility for 24 GeV protons and the CYRIC facility in Japan for 80 MeV protons. Table 1 lists the LGAD sensors measured in the beam tests, including the manufacturer, the sensor IDs, the implant of the multiplication layer as well as the irradiation type and fluence. It also includes the device name we assigned to each sensor for easier reference in the text and contains several information: the sensor type (Boron, Carbon, Gallium, 3.1 or 3.2), the geometry (single-pad or array), the irradiation level in units of $10^{14}\ \mathrm{n_{eq}}/cm^2$ and the type of particle that the devices were exposed to.

2.3 I-V and C-V measurements

Electrical measurements on the sensors were carried out prior to the beam test using a cooled probe station equipped with needle contacts. In order to study the gain layer V_{gl}, full depletion V_{fd} and breakdown V_{bd} voltages, the current-voltage (I-V) and the capacitance-voltage (C-V) scans were performed for each sensor with the guard ring grounded. Figure 3 shows the I-V characteristics for several tested sensors. The I-V measurements for both CNM and HPK sensors revealed a bulk leakage current of about 1 nA before irradiation. This value increases for irradiated sensors to about 0.1 µA and it is about two orders of magnitude higher for Gallium-type LGADs at lower fluences. For the unirradiated devices, V_{bd} is below 100 V at −30 °C for the CNM sensors, 140 V for HPK-3.2 and 270 V for HPK-3.1 at 20 °C. For HPK sensors the I-V curve was later measured at −30 °C, and V_{bd} was found to be 70 V for HPK-3.2 and 200 V for HPK-3.1 [4]. As expected, the breakdown voltage moves towards lower voltage values as the temperature decreases and it also moves towards higher voltage values as the fluence increases.

Table 1. List of CNM and HPK LGAD sensors studied in the 2018–2019 beam test periods: single-pads ("S") and arrays ("A") including the information on the implant of the multiplication layer, the irradiation level and type.

Device name	Manufacturer	Sensor ID	Implant	Irradiation type	Fluence [$\mathrm{n_{eq}}/cm^2$]
LGA35	CNM	W9LGA35	Boron	unirradiated	
Boron S	CNM	W4S1030	Boron	unirradiated	
Boron S1n	CNM	W4S1095	Boron	n	1×10^{14}
Boron S6n	CNM	W4S1016	Boron	n	6×10^{14}
Boron S1p	CNM	W4S1067	Boron	p	1×10^{14}
Carbon S	CNM	W5S1013	Boron+Carbon	unirradiated	
Carbon S1n	CNM	W5S1005	Boron+Carbon	n	1×10^{14}
Carbon S1p	CNM	W5S1038	Boron+Carbon	p	1×10^{14}
Gallium S	CNM	W6S1021	Gallium	unirradiated	
Gallium S1n	CNM	W6S1007	Gallium	n	1×10^{14}
Gallium S30n	CNM	W6S1006	Gallium	n	30×10^{14}
Gallium S1p	CNM	W6S1028	Gallium	p	1×10^{14}
3.1 A	HPK	3.1 W8 2x2 SE5IP3	Boron	unirradiated	
3.1 S8n	HPK	3.1 W8 P2LGE5	Boron	n	8×10^{14}
3.1 S10p	HPK	3.1 W8 LGE5	Boron	p	10×10^{14}
3.2 A	HPK	3.2 W18 2x2 SE5IP3	Boron	unirradiated	
3.2 S8n	HPK	3.2 W18 P4LGE5	Boron	n	8×10^{14}
3.2 A15n	HPK	3.2 W18 2x2 SE5IP3	Boron	n	15×10^{14}
3.2 S15n	HPK	3.2 SE3 (high gain)	Boron	n	15×10^{14}

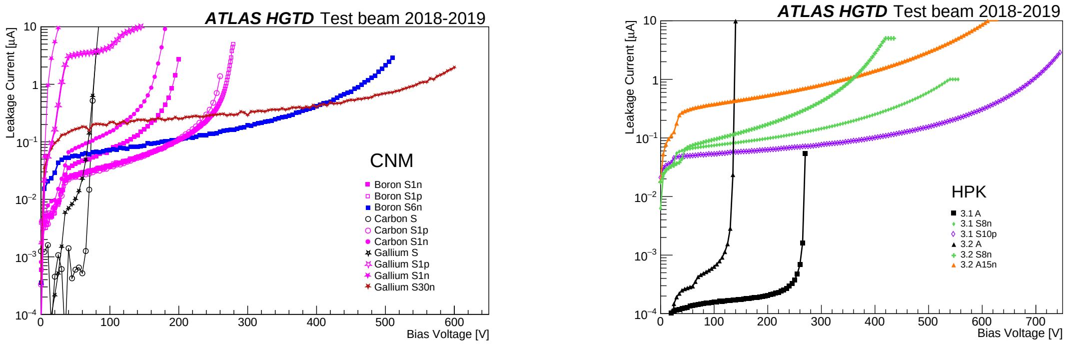

Figure 3. Leakage current-voltage dependence for CNM (left) and HPK (right) sensors. Note that all curves were performed at −30 °C except the two unirradiated HPK devices that were measured at 20 °C.

The C-V measurements in figure 4 show the V_{gl} and V_{fd} voltages for unirradiated HPK sensors. The V_{gl} is 40 V for HPK-3.1 and 55 V for HPK-3.2 and the V_{fd} is 50 V for HPK-3.1 and 65 V for HPK-3.2. This is explained by the difference in gain layer depth, as deeper is the gain layer more bias is required for the sensor to be fully depleted, which is the case of HPK-3.2. Similar measurements for CNM sensors showed equivalent V_{gl} and V_{fd} values below 50 V [17]. The detector capacitance was measured to be $C = 2.9$ pF for both CNM and HPK sensors.

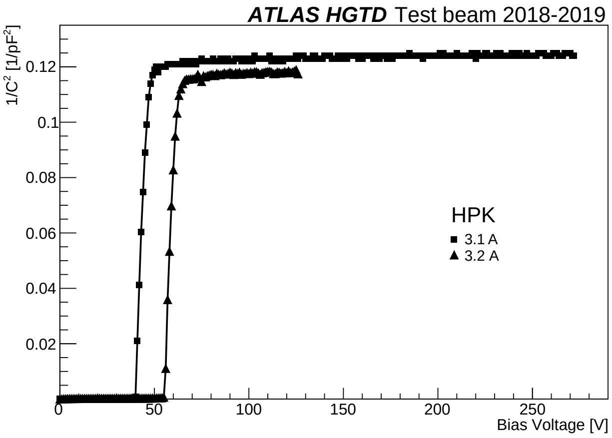

Figure 4. Capacitance-voltage dependence for unirradiated HPK sensors showing a full depletion voltage of 50 V for HPK-3.1 and 65 V for HPK-3.2.

3 Test beam set-up

The HGTD beam test campaigns were conducted at the CERN SPS [11] H6A line using a high-momentum 120 GeV pion beam and at the DESY [12] TB 22 line using a 5 GeV electron beam. The two set-ups are similar, but to reduce the multiple scattering at DESY the number of devices under test (DUTs) evaluated simultaneously was therefore reduced. At CERN, up to six DUTs were tested at the same time [13], placed in a thermally isolated enclosure where the temperature could reach −40 °C. Measurements were taken at −30 °C and −20 °C. At DESY, only three DUTs were tested simultaneously with a cooling system consisting of a styrofoam box with a separate compartment for the addition of dry ice packs [19]. The temperature was monitored with a Pt100 sensor and it was in the range of −40 °C to −25 °C. In both test beam infrastructures, for position-dependent measurements, a beam telescope [20] was used allowing the evaluation of sensor efficiency and charge uniformity as a function of the particle incident position. An independent time reference was provided to the data acquisition (DAQ) system by a Silicon Photomultiplier (SiPM) assembly [21].

3.1 Read-out electronics boards

LGAD sensors were assembled on 10 cm × 10 cm read-out and amplification boards using double-sided conductive tape. These boards were developed at the University of California Santa Cruz (UCSC) [22] in two versions: single-channel for single-pad LGADs and four-channel for 2×2 LGAD arrays. The LGAD front-side metal pad layer was coupled to the input of an on-board transimpedance first-stage amplifier via multiple wire bonds to reduce the inductance, while the guard ring was grounded. The single-channel version (figure 5 (left)) only includes this first amplification stage based on a single-transistor common emitter design that acts as an inverting transimpedance amplifier. For further amplification, it uses an external second-stage amplifier with hermetic E/B cover design from Mini-Circuits with a gain of about 10 and a 2 GHz bandwidth. The four-channel version (figure 5 (centre)) includes, in addition to the first amplification stage, two more amplifiers with a voltage divider between them resulting in a total gain of about 200 at a 1.6 GHz

2022 JINST 17 P09026

bandwidth. Both boards are equipped with SMA connectors providing low voltage input (2.25 V for the single-channel version, or 5 V for the four-channel version), one amplifier output (which goes to the external second-stage amplifier in the single-channel version) or four amplifier outputs (four-channel version), a calibration line input and a high-voltage input for reverse biasing the LGAD from the back of the sensor. The amplifier outputs were connected to the oscilloscope to record the LGAD signal. A third type of board developed at the University of Kansas (KU) was also used to test two 2×2 DUTs, 3.1 A and 3.2 A (figure 5 (right)). This KU board [23, 24] is a two-channel version and is equipped with a 2-pin connector providing low voltage input, two SMA connectors providing two amplifier outputs and a LEMO connector serving as high-voltage input. It includes two identical two-stage transimpedance amplifiers.

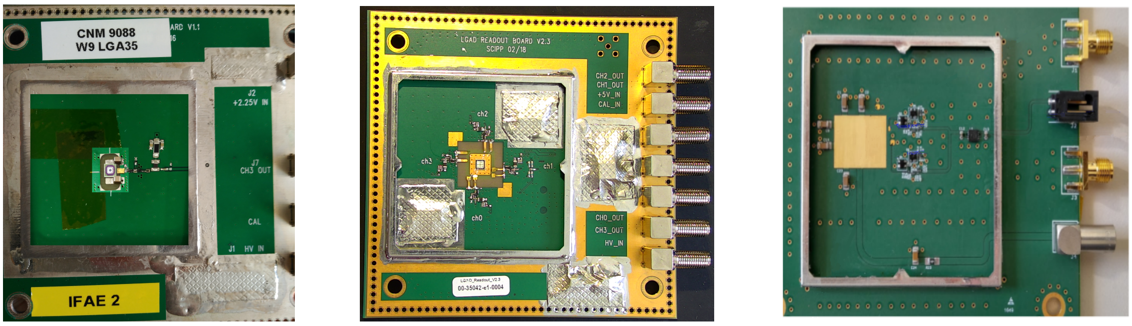

Figure 5. LGAD read-out boards: UCSC single-channel version (left), UCSC four-channel version (centre) and KU two-channel version (right).

3.2 Time reference system

In order to perform timing measurements with the DUTs, a time reference system with a resolution similar or better than that of the DUT is needed. The chosen system [21] consists of a SiPM coupled to a quartz bar assembled in a light-tight housing. The full assembly is attached to a custom read-out board designed at Institut de Física d'Altes Energies (IFAE). The measured time resolution from this time reference system was found to be 39.0(22) ps for an operating voltage of 27.8 V. After hundreds of hours in operation and under beam exposure in several beam tests, an increase of the SIPM leakage current was observed. Thus, a reduced voltage of 27.6 V was applied and the corresponding time resolution was found to be 63.3(9) ps. This time reference system was tested together with the DUTs and with an additional unirradiated LGAD, LGA35 (see table 1), which has a well known performance and it was also used as a reference in the evaluation of the time resolution performances (see section 5).

3.2.1 Quartz bar

A 6-side polished quartz bar of size $3 \times 3 \times 10\,\text{mm}^3$ was used as a medium where the traversing charged-particles generate photons through the Cherenkov effect. In order to maximize the photon transmission efficiency, the chosen quartz is suitable for ultraviolet (UV) light where the Cherenkov spectrum peaks. A transparent optical grease[3] was selected for the interface quartz-SiPM window which is also optimized for blue light detection [25].

---

[3] Bluesil Paste 7 from Silitech AG.

3.2.2 SiPM

A SiPM detector[4] was chosen due to its extremely high sensitivity, high efficiency and very low time jitter. It has an active area of 3 mm × 3 mm made of 50 µm micro-cells interconnected in a parallel manner [26], providing a 72% fill factor. The sensor is encapsulated on a 4 mm × 4 mm × 0.7 mm-thick SMT package [25] and is integrated in an evaluation board which can be easily mounted via pin headers (figure 6) [27]. This design allows a fast replacement which is useful, since after its use in several beam test campaigns its performance degrades due to the particle fluence.

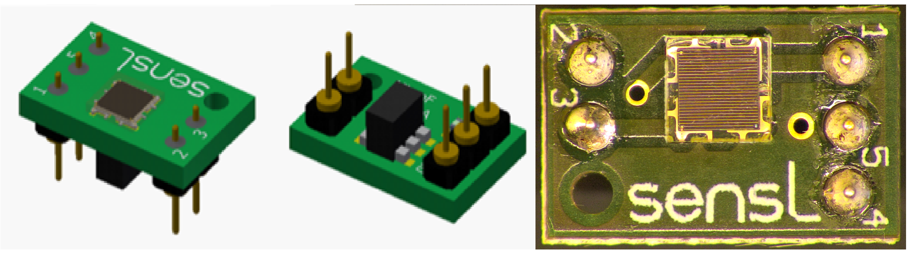

Figure 6. SiPM evaluation board (3D schematics and picture).

3.2.3 Light-tight support

The SiPM and the quartz assembly needed both mechanical support and optical isolation from the environment to achieve efficient photon detection. A light-tight enclosure was designed at IFAE and 3D printed using black PLA plastic with a 90% fill factor at IJCLab. The support as shown in figure 7 consists of two parts:

- a main cubic unit with a hole allowing the insertion of the quartz bar and the attachment via a screw of the SiPM evaluation board at the back face
- a cover for fixation via two screws and optical isolation of the quartz bar at the front face

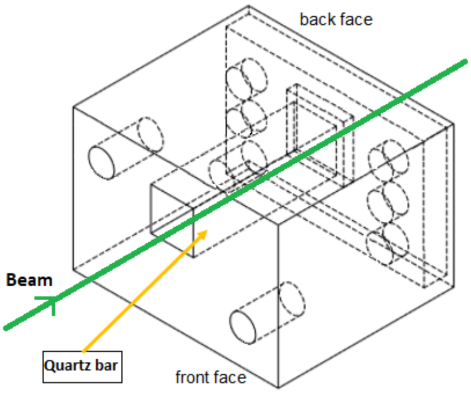

Figure 7. SiPM light-tight support design of main unit.

---

[4] MicroFC-30050-SMT model from SensL Technologies TM.

3.2.4 Read-out board

The SiPM evaluation board does not include any amplification stage. Therefore, a read-out board was designed at IFAE for this purpose using a commercial amplifier [28], providing a 2 GHz bandwidth with a gain of 10 at nominal operating voltage (12 V). In addition, the position of the SiPM-quartz assembly in the board was chosen to be aligned with the LGADs on their respective read-out boards. In order to avoid high-frequency electromagnetic interference a metal shield enclosing the amplifier and filtering circuitry was added (figure 8 (left)).

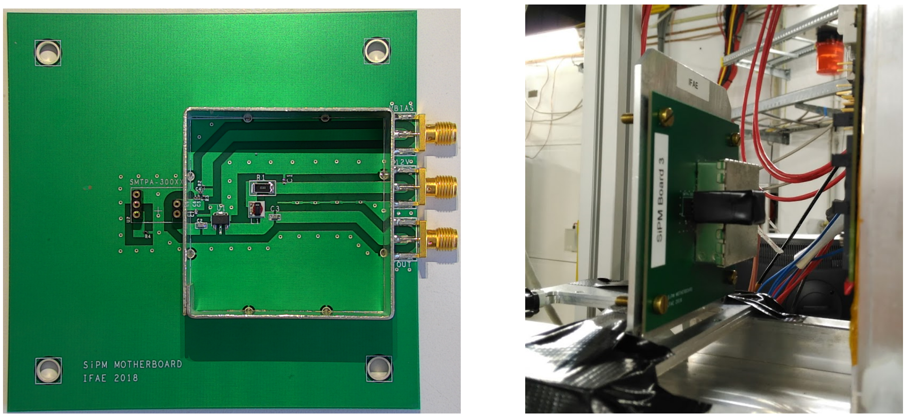

Figure 8. SiPM PCB without metal cover (left) and full assembly at the test beam (right).

3.3 Beam tracking system

The alignment of the DUTs was provided by custom-made L-shape supports where the LGAD read-out boards could be mounted back-to-back in pairs on a base plate. As explained earlier, at CERN, the set-up was placed in a thermally isolated enclosure whereas at DESY it was mounted on a light-tight cooling box. In both cases, the position of the assembly was remotely controlled by a micrometric x-y motor stage in the perpendicular plane to the beam axis (z direction). In this way, DUTs were precisely positioned inside the beam profile of a size of about $2 \times 2\,\text{cm}^2$. Position-dependent measurements were possible to perform with the use of a EUDET-type telescope [20] consisting of two equidistant arms, each comprised of three MIMOSA pixel planes. Each MIMOSA plane has an area of $10.6 \times 21.2\,\text{mm}^2$, and is composed of pixels with a size of $18.5 \times 18.5\,\mu\text{m}^2$, providing particle track information with a resolution of a few micrometers. DUTs were placed in the space available between the two telescope arms as shown in figure 9. Two intersecting plastic scintillators coupled to photomultiplier tubes were also integrated at each extremity of the telescope and used in the trigger scheme. An additional pixel reference plane, using the FE-I4 [29] read-out chip, was also positioned at the end of the second telescope arm and served for DUT alignment as well as for triggering purposes. The dimension of the FE-I4 plane is $16.8 \times 20.0\,\text{mm}^2$ with a pixel size of $50 \times 250\,\mu\text{m}^2$. The time reference system described before was placed after the pixel reference plane. At CERN, this system was mounted outside the telescope structure and it was aligned with respect to the beam by using a remote control positioning stage[5] whereas at DESY it was mounted directly on the telescope structure, being already aligned with the MIMOSA and pixel reference planes.

---

[5] Stage system from Physik Instrumente (PI).

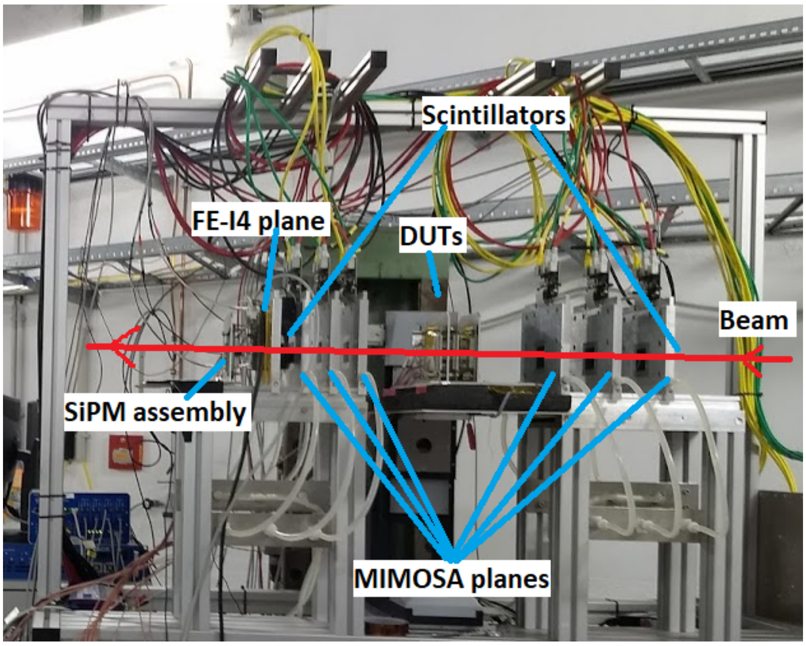

Figure 9. Beam telescope infrastructure at DESY including scintillators for triggering, a pixel reference plane, a time reference system based on a SiPM and LGAD sensors as DUTs.

2022 JINST 17 P09026

3.4 Data acquisition and trigger scheme

Signals from DUTs were registered by a four-channel oscilloscope (first 3 channels for DUTs and a fourth channel for the time reference signal coming from the SiPM assembly). In the case of data-taking at CERN, two identical 10 GS/s synchronized oscilloscopes with a 2 GHz bandwidth were used, each of them with an input of a time reference signal from two identical SiPM systems. For data-taking at DESY, only one oscilloscope was used since only three DUTs were tested simultaneously in order to reduce the multiple scattering.

The trigger and DAQ architecture is presented in figure 10 (top). A region of interest (ROI) on the FE-I4 plane that contained the projected area of the different LGADs and SiPM was defined. It is critical to have an optimal alignment of all the LGADs and the SIPM in order to perform time measurements. The typical size of the ROI was about the SIPM size, 3 mm × 3 mm. Thus, the implementation of this ROI resulted in a reduced hit rate. The downstream intersecting scintillators in the telescope, the HitOR signal from the FE-I4 plane and the oscilloscope auxiliary output were the input to the EUDET Trigger Logic Unit (TLU) [30]. The oscilloscope needed to have sufficient time offset in order to record the signal that arrived previous to the trigger. When the oscilloscope is triggered through the EXT signal coming from the TLU (event), it emits a TTL pulse that is sent back to the TLU module for synchronization of the telescope and FE-I4 DAQ system (NI-Crate using EUDAQ [31] and USBPix/MMC3 [32]) with the HGTD DAQ system (oscilloscope). The oscilloscope has a dead time of approximately 10 s caused by the buffer read-out, which at CERN SPS was granted by the time in between spills (about 4 s-long, every 16 s). At DESY, a NIM logic circuit was implemented to generate a busy signal (20 ns-long veto pulse) from the oscilloscope for the TLU. Figure 10 (bottom) shows the busy signal implementation scheme.

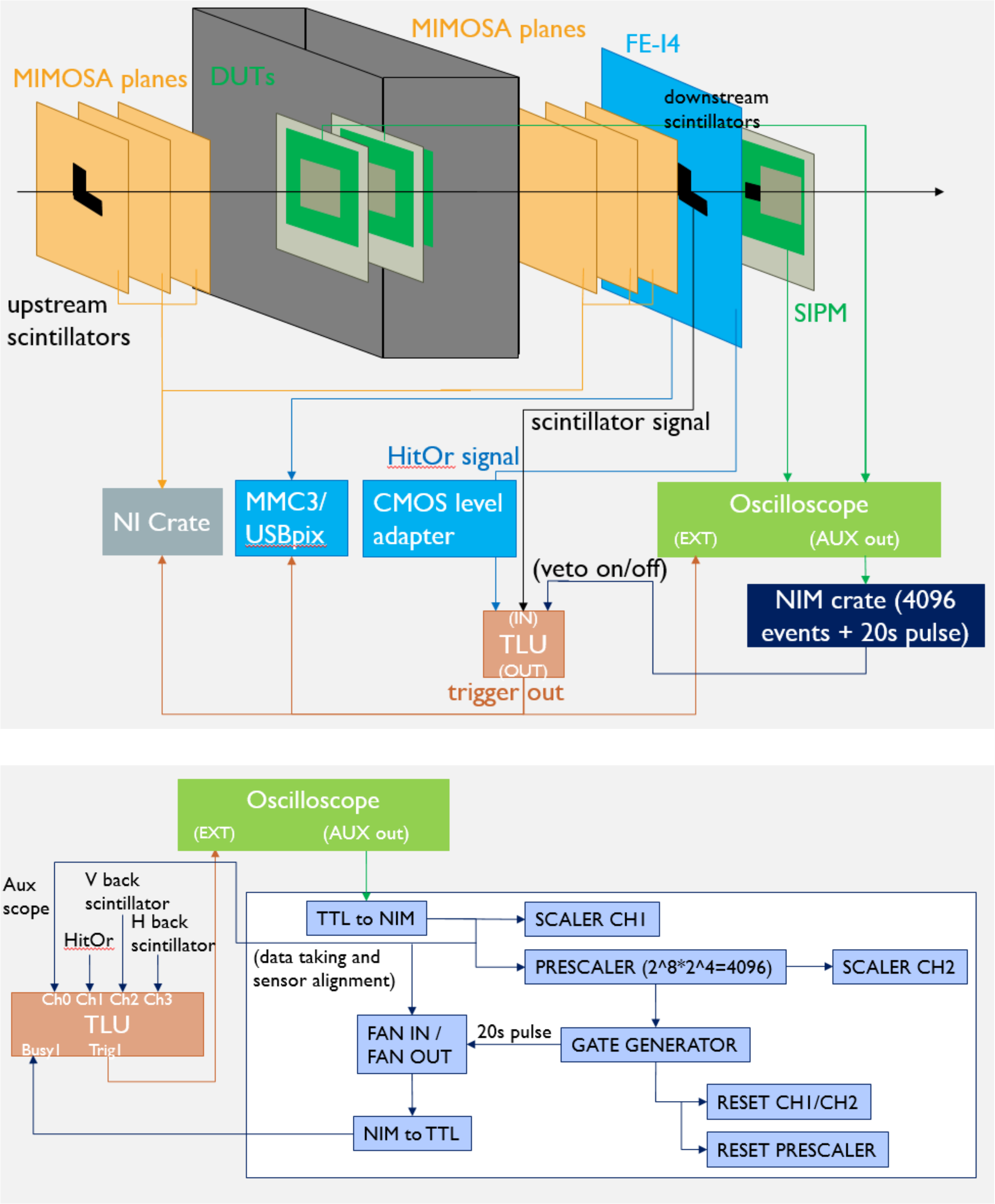

Figure 10. DAQ and trigger scheme (top) and busy signal scheme (bottom).

Two independent data streams were recorded, one containing particle position information from the telescope and the FE-I4 while the second containing waveform signals from the DUTs registered by the oscilloscope. These two data streams were merged offline for further analysis (see sections 4 and 5).

4 Data analysis approach

As mentioned in the previous section, two independent systems were used to collect the data used in this analysis: the oscilloscope provided data on the LGAD and SIPM waveforms while the telescope on the particle track information. This section describes the general methodology used to reconstruct and process the information from these two chains, and how it was used to derive the physical quantities of interest for the analysis.

4.1 Waveform processing

This procedure is described in several steps as it is done in [33]. The first step was to convert the oscilloscope binary data into a ROOT ntuple containing the raw waveform information of each DUT which were sampled with a time bin of 25 ps. Figure 11 shows a typical LGAD signal. The second step was the determination of the pulse polarity, the maximum, the minimum, the start and the stop points of the signal. With this information, a check if the complete pulse was within the oscilloscope acquisition window was made. The third step was to compute the pedestal and the noise in the range from the 10 % to 90 % points before the start of the pulse. They were defined as the mean and the standard deviation of a Gaussian fit, respectively. Subsequently, the value obtained for the pedestal was subtracted from all the data points of the waveform, on an event-by-event basis. The minimum, maximum, start and stop points were then re-calculated. The maximum of the waveform was determined from the sample with the highest amplitude. The fourth step was the computation of several waveform properties such as the charge, the rise time, the jitter, the signal-to-noise ratio and the Time Of Arrival (TOA) at different thresholds.

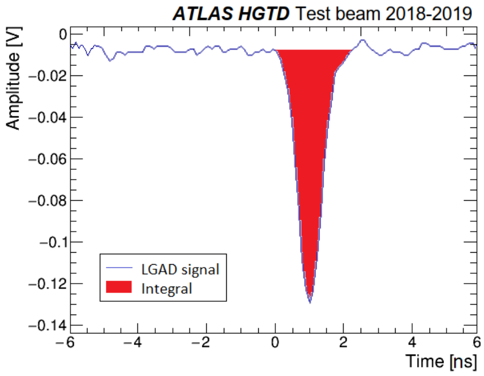

Figure 11. Recorded waveform from an LGAD. The integral of the signal is denoted by the red area.

For each event, the charge, q, was determined by dividing the integral of the pulse (see figure 11) by the transimpedance of the read-out board, R_b, and the gain of the voltage amplifier, G_{ampl}:

$$q = \frac{\int_{\mathrm{start}}^{\mathrm{stop}} A\,dt}{R_b \times G_{\mathrm{ampl}}} \tag{4.1}$$

While several methods to reconstruct the TOA have been studied in a previous paper [13], the analysis presented in this paper uses the Constant Fraction Discriminator (CFD) method: the TOA is defined as the point in which the signal crosses a predefined fraction, f_{CFD}, of its total amplitude. To obtain the time resolution, the TOA value at $f_{\mathrm{CFD}} = 20\%$ will be used for the time references and the unirradiated DUTs whereas for the irradiated DUTs the TOA value will be at $f_{\mathrm{CFD}} = 50\%$. The impact of this choice on the time resolution estimate is discussed in section 5.2.1.

The last step was to produce a merged file containing the oscilloscope data together with the telescope reconstructed data (see next section) for the user analysis.

4.2 Track reconstruction

The telescope together with the FE-I4 provided the tracking information that allowed to reconstruct the trajectory of the particles and to identify the specific position where the DUT has been hit. The tracking capability of the telescope was provided by six MIMOSA planes as explained in section 3.3. The positions of the MIMOSA, FE-I4 and DUT planes were known with a precision of 1 mm in the z direction along the beam line. The position of the hits from each MIMOSA plane, together with their respective z coordinate, were used to reconstruct the particle trajectory and the (x, y) coordinates of the hit on the DUT planes.

After the removal of "hot" pixels from the MIMOSA planes, identified as the ones with an occupancy higher than ten times the average one, the remaining hits were grouped into clusters. Only clusters with a maximum of 6 hits were used for tracking. In the FE-I4 plane, a cluster was required to have a maximum of 2 neighbouring hits. The cluster coordinates were the centroid of the hit coordinates in x and y. Only events with exactly one cluster in the FE-I4 were then considered. The MIMOSA planes were aligned by iteratively shifting the planes coordinates in x and y direction with respect to a reference plane. This procedure aimed to minimize the difference between the reconstructed track position at the MIMOSA plane and the measured hit position in the same plane. The position resolution was taken as the resolution of the fit performed during the alignment procedure.

For data collected at CERN SPS, the following track fitting procedure was applied. Given the z position of the MIMOSA planes along the beam axis and the x and y positions of the hits in these planes, 3D-tracks were built from the six planes of the telescope starting with the planes closest to the FE-I4 [13]. The reconstructed tracks must coincide with a hit in the FE-I4 plane and only events with a single reconstructed track through the six MIMOSA planes were considered. The track fitting procedure was slightly different for data collected at DESY in order to take into account the differences in the experimental set-up and the beam type. The tracking procedure was initialised in the upstream MIMOSA planes, and no matching requirement between the extrapolated track and the FE-I4 cluster was applied [34, 35]. Events with more than one candidate track were retained if the candidate tracks were compatible with kinks from multiple scattering from a single track.

Once the tracks have been reconstructed, their trajectory was evaluated at the z coordinate of the DUTs, to determine the (x, y) coordinates of the hit and this information was saved into a file. The precision on the position of the extrapolated reconstructed track in the DUT planes was about 3 µm in the x and y directions.

5 Sensors performance results

The studies presented in this paper aim to evaluate the LGAD sensor performances, before and after irradiation, with particle beams using the reconstructed position of the tracks. The following

LGAD properties have been investigated: the collected charge, the time resolution and the hit reconstruction efficiency.

In the subsequent analyses, two type of cuts were applied to remove the background events (figure 12): a geometrical cut based on the position where the DUT or the time references (LGA35, SIPM) were located inside the FE-I4 ROI, and a timing cut using a 2 ns window from the maximum point of the time difference distribution between the TOA of the DUT and SIPM read out by the same oscilloscope. As mentioned in section 4, the TOA was determined for all of the devices with the CFD method, where the values at $f_{\mathrm{CFD}} = 20\%$ for the unirradiated DUTs and the references and at $f_{\mathrm{CFD}} = 50\%$ for the irradiated DUTs were considered. Figure 12 shows the reconstructed tracks inside the FE-I4 ROI at the DUT plane before (left) and after (right) the timing cut (centre). After applying the cleaning selections in geometry the retained events correspond to reconstructed tracks inside the FE-I4 ROI that are crossing the DUT.

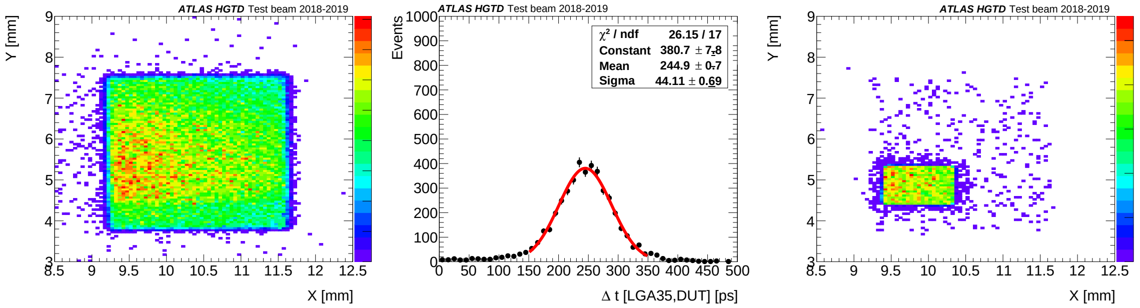

Figure 12. Reconstructed tracks inside the FE-I4 ROI at the DUT plane before (left) and after (right) a timing cut was applied. Time difference distributions between the DUT and LGA35 (centre).

To guide the interpretation in terms of irradiation fluence, in the presented figures points corresponding to the same fluence will be shown in the same color. Solid markers correspond to neutron irradiation and empty markers correspond to proton irradiation. Black points either solid or empty markers correspond to unirradiated DUTs.

5.1 Collected charge

From the retained events after applying the cleaning cuts, a distribution using the charge derived from Equation 4.1 was obtained for each DUT and it was fitted with a Landau-Gaussian convoluted function. The collected charge reported for each sensor is defined as the Most Probable Value (MPV) from this fit and designated as $\mathrm{Charge}_{\mathrm{MPV}}$ for later calculations. As an example, figure 13 shows a charge distribution of Carbon S1p operated at a bias voltage of 220 V, before (left) and after (right) the cleaning selections. Figure 13 (right) also includes the resulting fit function with an MPV of 9.8 fC. The negative charge remaining after the cleaning cuts results from noise events or fluctuating signals from particles hitting the edge of the sensor.

Figures 14 and 15 show the results for CNM and HPK sensors, respectively. Unirradiated sensors always have high collected charge, even if they are operated at low bias voltages. Irradiated sensors yield a lower collected charge than unirradiated devices at the same bias voltage and they require a higher bias voltage to obtain a similar performance. The gain of the sensors is reduced with the irradiation, the higher the fluence the higher the bias voltage needed to obtain the minimum

2022 JINST 17 P09026

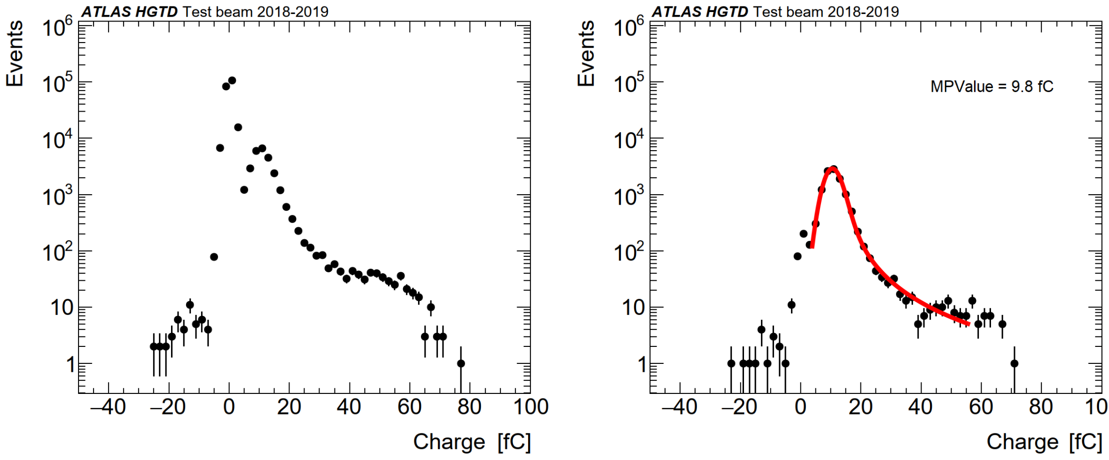

Figure 13. Charge distribution for Carbon S1p operated at a bias voltage of 220 V before (left) and after (right) cleaning cuts. The right figure also includes the Landau-Gaussian fit.

required charge of 4 fC to provide a good timing. The three types of CNM sensors were irradiated at a fluence of 10^{14} n_{eq}/cm^2 with neutrons (S1n DUTs) and protons (S1p DUTs). By comparing them, neutron-irradiated DUTs show a better performance at the same bias voltage. In particular, Carbon S1n collects more charge than Boron S1n whereas Gallium S1n need more voltage to get the same amount of charge. This is in agreement with laboratory data [36]. Unirradiated DUTs, Boron S6n and Gallium S30n were not operated at higher voltages to prevent the early death of the sensor. For HPK sensors, 3.2 A does not perform properly at low temperature and could not be operated at voltages higher than −70 V because it presented self-triggering [4, 36]. However, after irradiation type-3.2 performs better than type-3.1 as it is seen in the case of 3.2 S8n which requires less voltage to achieve the same performance than 3.1 S8n. Type-3.2 has a deep and high-dose multiplication layer, which leads to a reduced acceptor removal rate. Therefore, the gain is higher at the same voltage for the same irradiation level. Figure 15 for HPK 3.2 sensors is in agreement with figure 5.8 (a) in [4].

5.1.1 Uniformity

In order to study how uniform is the charge within the pad of the sensors, a two-dimensional (2D) map of the occupancy as a function of the reconstructed particle position in the DUT plane was built. To increase the number of events and provide a simpler interpretation of the results, the uniformity of the charge was evaluated in the x-axis while integrating over the y-axis. This was done by dividing the sensor active area into ten bins of 0.1×1 mm^2 as shown in figure 16 (left). The collected charge in each bin k, Charge$_{MPV_k}$, was computed. As an example, figure 16 (right) shows the charge distribution in one bin together with the Landau-Gaussian function fit for DUT Carbon S1p.

The uniformity of the charge was evaluated for each DUT at the maximum applied voltage. As shown in figures 14 and 15, the collected charge varies with the bias voltage and with the irradiation level. In order to compare sensors with different collected charge, the value computed in each bin is normalized to the collected charge of the sensor. Thus, the uniformity of the charge along the x-axis

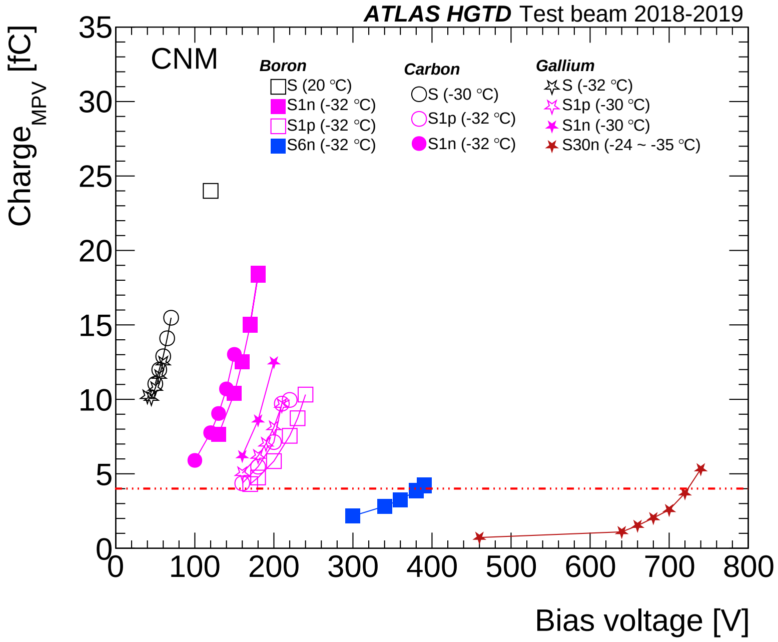

Figure 14. Collected charge as a function of the bias voltage for CNM Boron, Carbon and Gallium sensors. The horizontal line represents the HGTD requirement of a minimum collected charge of 4 fC.

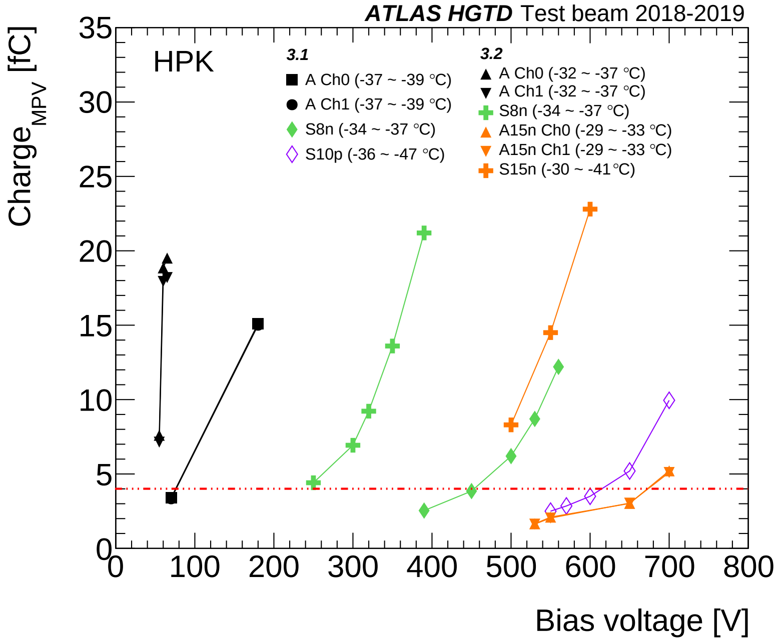

Figure 15. Collected charge as a function of the bias voltage for HPK 3.1 and 3.2 sensors. The horizontal line represents the HGTD requirement of a minimum collected charge of 4 fC.

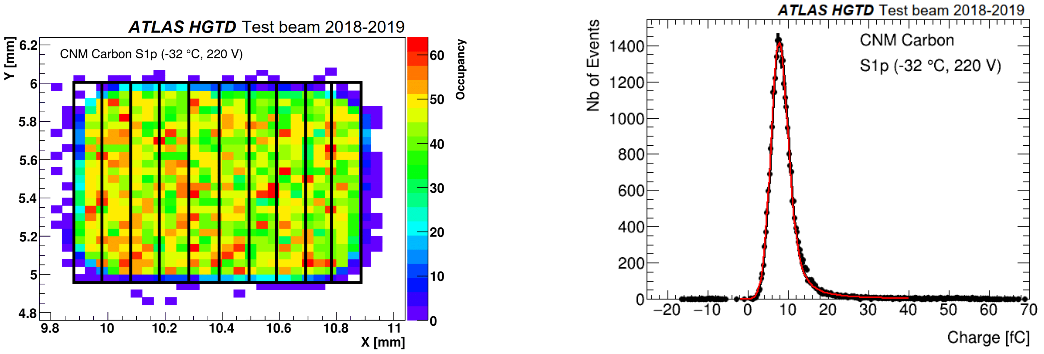

Figure 16. 2D map of the hit occupancy as a function of the reconstructed particle position in the DUT plane for Carbon S1p operated at a bias voltage of 220 V (left). The black boxes correspond to the bins along x-axis. Charge distribution computed in a bin size of 0.1×1 mm^2 (right).

is calculated as a relative charge defined by:

$$\text{Relative Charge} = \frac{\text{Charge}_{\text{MPV}_k}}{\text{Charge}_{\text{MPV}}} \tag{5.1}$$

Figure 17 shows the uniformity for the CNM sensors while figure 18 shows for the HPK ones. The uniformity in the y-axis was also checked and was found to be similar. Small deviations are observed for the unirradiated and low-fluence CNM sensors. The uniformity of Carbon S1p shows larger deviations, which stay within 10% of the average and therefore are not considered significant. Similarly, the uniformity of Gallium S30n presents a spread within 5% in most of its surface. The tested HPK sensors show a very good uniformity at all fluences. At the highest fluence, for A15n-ch0 the relative charge decreases at the edges much more than for the other DUTs. In general for both vendors, larger deviations can be appreciated in the periphery of the sensors due to edge effects.

5.2 Time resolution

The time resolution is one of the key parameters when assessing the sensor performance. It can be determined by:

$$\sigma^2_{\text{LGAD}} = \sigma^2_{\text{Landau}} + \sigma^2_{\text{Time walk}} + \sigma^2_{\text{Jitter}} \tag{5.2}$$

The Landau fluctuations, σ_{Landau}, are caused by non-uniformities in energy deposition along the particle path inside the sensor. While this effect is reduced decreasing the thickness of the sensor, thinner sensors suffer from large capacitance and low deposited charge. Therefore, a compromise must be made. The time walk effect, $\sigma_{\text{Time walk}}$, is explained by the fact that signals with different amplitudes reach a fixed discriminator at different times. This effect can be mitigated by using specific reconstruction techniques. The jitter term, σ_{Jitter}, is instead proportional to the presence of electronic noise and to the rise time, while it is inversely proportional to the signal slope.

For all the combinations of DUTs and references tested simultaneously, a distribution of the TOA differences can be built and used to extract the DUT time resolution. The width of the time difference distribution between device i and j will be given by:

$$\sigma_{i,j} = \sigma_i \oplus \sigma_j \tag{5.3}$$

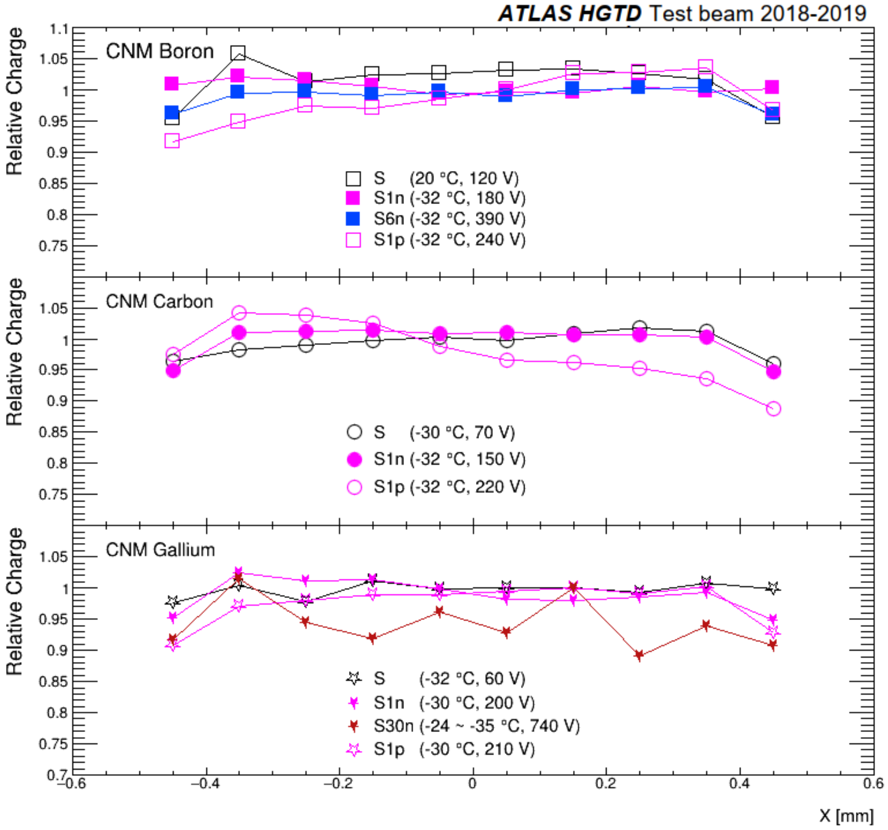

Figure 17. Relative charge along the x-axis for CNM Boron, Carbon and Gallium sensors, indicating the temperature and the bias voltage of operation.

where σ_i and σ_j are the individual time resolutions of the two devices, and $\sigma_{i,j}$ is estimate as the width of a Gaussian function fit.

When exactly three devices are considered, it is possible to solve the system of three equations and derive the individual time resolutions by measuring the resolution of several time differences. For example, considering two references and a DUT, the time resolution of the DUT can be extracted as:

$$\sigma_{\text{DUT}} = \sqrt{\frac{\sigma^2_{\text{DUT-Ref1}} + \sigma^2_{\text{DUT-Ref2}} - \sigma^2_{\text{Ref2-Ref1}}}{2}} \tag{5.4}$$

When more than three devices are considered simultaneously, the system is over-constrained and one way to determine the value of the individual time resolutions is through a χ^2 minimization:

$$\chi^2 = \sum_{i=1}^{N} \sum_{j=1}^{j<i} \frac{(\sigma^2_{ij} - \sigma^2_i - \sigma^2_j)^2}{\sigma^2_{\sigma^2_{ij}}} \tag{5.5}$$

For each DUT, the two references (LGA35 and SIPM) were used to compute its time resolution using eq. (5.4). An example of a time difference distribution together with the Gaussian fit function used to extract the resolution was shown in figure 12 (centre).

Figures 19 and 20 show the time resolution as a function of the bias voltage for CNM and HPK sensors, respectively. Both figures show an improvement of the time resolution with higher bias

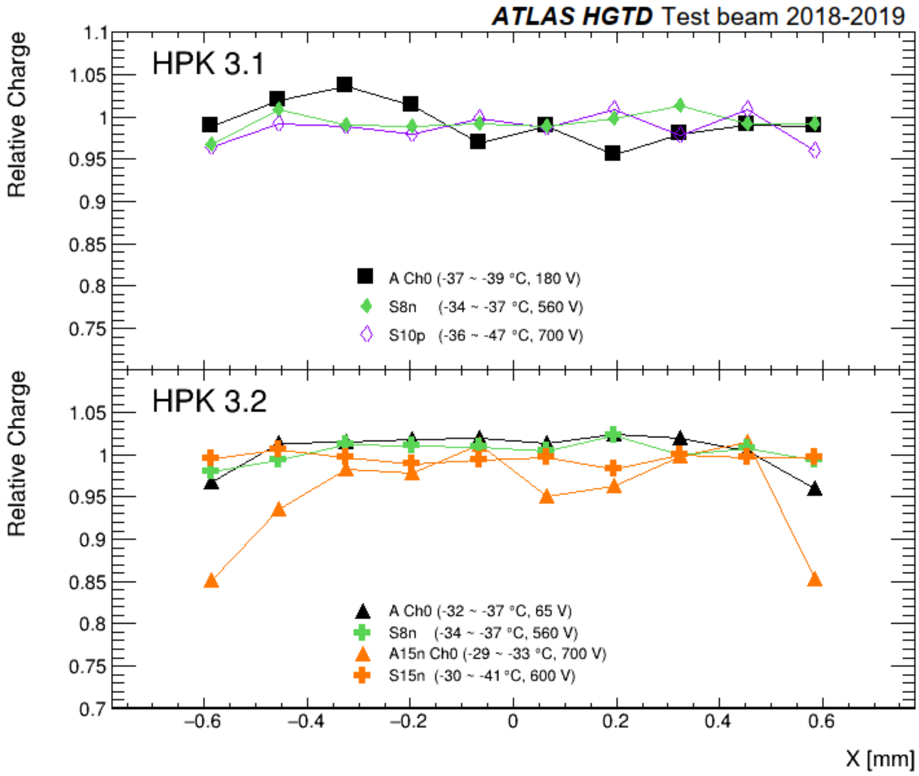

Figure 18. Relative charge along the x-axis for HPK 3.1 and 3.2 sensors, indicating the temperature and the bias voltage of operation.

voltages. For Gallium sensors in figure 19, at 200 V, both neutron- and proton-irradiated at a fluence $10^{14}\,\mathrm{n_{eq}/cm^2}$ were tested. DUT Gallium S1n achieves a time resolution of 27.4 ps, this type of radiation therefore causing less damage than the proton one, for which DUT Gallium S1p achieves a time resolution of 38.3 ps at the same bias voltage. The same conclusion can be obtained for Carbon sensors in the bias voltage range of 150 V to 160 V, where both neutron- and proton-irradiated sensors were tested and the neutron-irradiated one shows a better performance.

Gallium S30n reaches the target time resolution at expenses of being operated at a rather high voltage. Detailed studies on the uniformity of the time resolution within the pad for this sensor are included in [19].

Figure 20 for HPK 3.2 sensors is in agreement with figure 5.11 (a) in [4]. At $8{\times}10^{14}\,\mathrm{n_{eq}/cm^2}$, HPK 3.2 performs better than HPK 3.1. For HPK sensors, a conclusion on the impact of the irradiation type on the sensor performance cannot be made. DUT 3.2 S8n achieves the best resolution of about 30 ps at 400 V.

The time resolution together with the collected charge obtained in section 5.1, allow to define the best operating voltage point for each sensor and irradiation level. Looking at these two key parameters in figure 21, only for irradiated DUTs from both vendors, all sensors follow the same trend. This figure is in agreement with figure 5.8 (a) in [4] for HPK 3.2 sensors. The plot is divided into four regions where LGADs meeting the HGTD requirements in terms of collected charge > 4 fC and time resolution < 70 ps appear in the bottom right area.

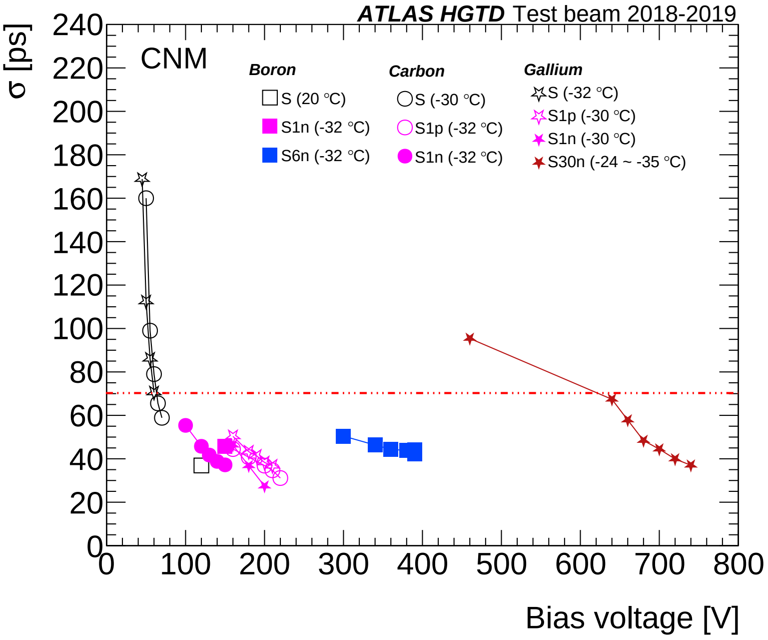

Figure 19. Time resolution as a function of the bias voltage for CNM Boron, Carbon and Gallium sensors.

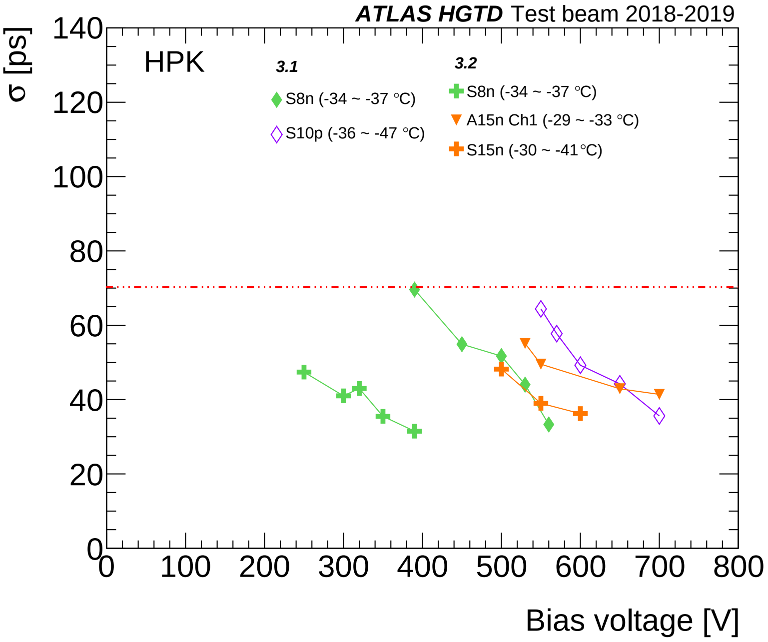

Figure 20. Time resolution as a function of the bias voltage for HPK 3.1 and 3.2 sensors.

5.2.1 Impact of the CFD fraction

A study of the time resolution variation for different CFD fractions is presented. The results of this study are used to determine if the CFD fractions, 20% for unirradiated DUTs and references

2022 JINST 17 P09026

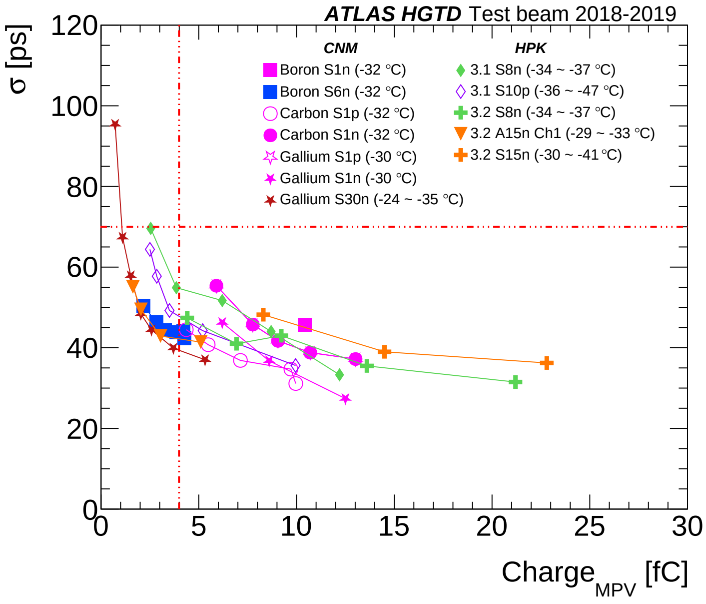

Figure 21. Time resolution as a function of the collected charge for irradiated CNM and HPK sensors.

and 50% for the irradiated DUTs, used to calculate the time resolutions in this paper are indeed the optimal values achieving the best time resolution. The calculation is carried out by repeating the computation of the time resolution (following the same procedure as for the results in section 5.2) changing each time the fraction used in the CFD method for the DUT and using eq. (5.5).

Figure 22 and figure 23 show the time resolution as a function of the DUT CFD fraction for CNM and HPK sensors, respectively. For the unirradiated sensors the Landau term dominates the time resolution and a low CFD fraction is preferred. For DUT Carbon S1p, the time resolution is significantly better compared to the DUT Gallium S. The Landau term still dominates the time resolution and a low CFD fraction is also preferred. HPK sensors were irradiated at a higher fluence up to 10^{15} n_{eq}/cm^2. Given the higher noise in these sensors, the effect on the time resolution of the jitter term becomes larger. The measured time resolutions varied from 1.20% to 11.99% for various HPK sensors with CFD fraction in the range from 30 % to 60 %. This interval is identified as the optimal range of CFD fraction for HPK sensors. The 50% CFD fraction used for the DUTs is within the optimal range of CFD fraction for HPK sensors. The fraction of 20% used for the SiPM and for the LGA35 is the optimal fraction for the unirradiated devices. The unirradiated, or with low fluence, CNM sensors results in 5 to 20% change of measured resolution when compared to resolution for the optimal CFD fraction.

5.3 Hit reconstruction efficiency

The hit reconstruction efficiency is defined as the reconstructed tracks giving a signal on the sensor for which the charge in the sensor is greater than a given threshold value, Q_{cut}, divided by the total number of reconstructed tracks crossing the sensor:

$$\text{Hit Efficiency} = \frac{\text{Reconstructed tracks with } q > Q_{\text{cut}}}{\text{Total reconstructed tracks}} \tag{5.6}$$

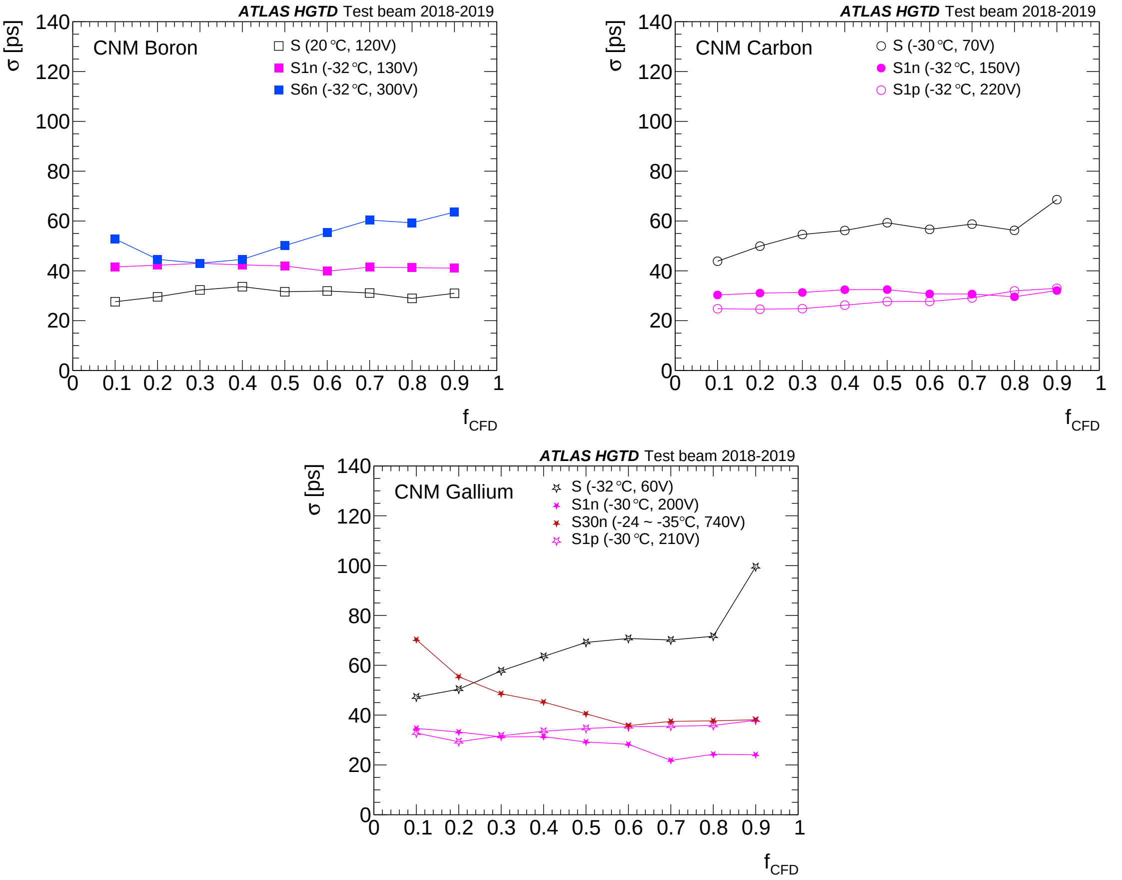

Figure 22. Time resolution as a function of the CFD fraction for CNM Boron (left), Carbon (right) and Gallium (bottom) sensors.

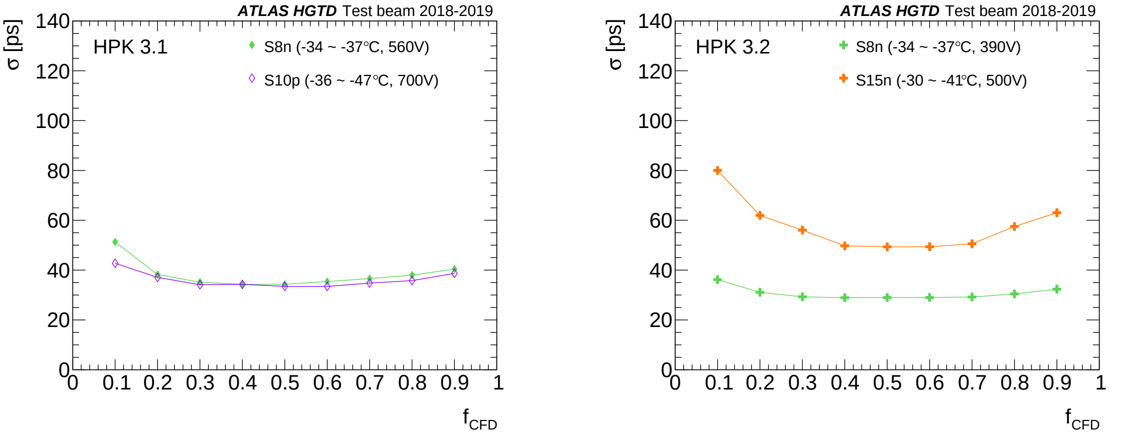

Figure 23. Time resolution as a function of the CFD fraction for HPK 3.1 (left) and 3.2 (right) sensors.

To avoid the effect of the sensor edge, the global efficiency values are computed in the central $0.5 \times 0.5\,\mathrm{mm}^2$ region of the DUT, representing a quarter of its surface for the CNM sensors and less than a quarter of its surface for the HPK sensors.

The efficiency as a function of the charge threshold at the highest operating voltage is shown in figures 24 and 25 for CNM and HPK sensors, respectively. DUTs do not get the same amount of charge at their maximum operating voltage, thus, the charge threshold results in a more dramatic efficiency drop in the cases with low collected charge. This is the case of DUTs irradiated with a fluence greater than $6 \times 10^{14}\,\mathrm{n_{eq}/cm^2}$, where the efficiency decreases as the charge threshold increases. This can be seen in figure 24 for Boron S6n where the efficiency decreases from 99.7% to 52.4% at 390 V when the charge threshold varies from 0.5 fC to 5 fC. In this case, the sensor was operated at a moderate voltage and the collected charge was rather low (4.26 fC). Similarly, for Gallium S30n the efficiency decreases from 99.9% to 74.7% at 740 V when the charge threshold varies from 0.5 fC to 5 fC, where the collected charge is 5.31 fC. For less irradiated DUTs, the efficiency as a function of the collected charge threshold is more constant as can be seen for other DUTs represented in figure 24. In the case of HPK sensors in figure 25, the efficiency for both type-3.1 and type-3.2 has a more constant behaviour as the charge threshold increases. At higher fluences, $1.5 \times 10^{15}\,\mathrm{n_{eq}/cm^2}$, for DUT 3.2 A15n the efficiency decreases as the charge threshold increases because of its low collected charge of about 5 fC whereas for DUT 3.2 S15n the efficiency remains constant as its collected charge is 22.76 fC.

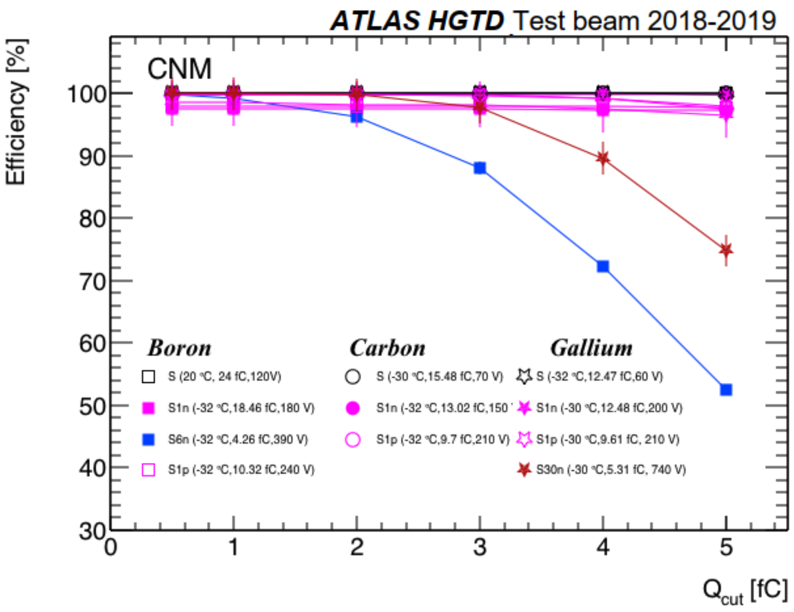

Figure 24. Efficiency as a function of the charge threshold for CNM Boron, Carbon and Gallium sensors.

An efficiency larger than 95% is reached for all the sensors up to a fluence of $3 \times 10^{15}\,\mathrm{n_{eq}/cm^2}$ for a charge threshold of 2 fC, corresponding to the discriminator of the ALTIROC.

In order to study the uniformity of the efficiency within the sensor, the efficiency was determined as a function of the hit position of the track on the sensor. In the following studies, the charge threshold was set to 2 fC for all sensors. Figure 26 (left) shows the 2D map of the efficiency as a function of the hit position in DUT Carbon S1p and figure 26 (right) in DUT 3.1S10p. On the left plot, the sensor was tested at CERN SPS with a 120 GeV pion beam and using a thermally isolated enclosure with a well stabilized position in x-y plane whereas the sensor on the right plot was tested

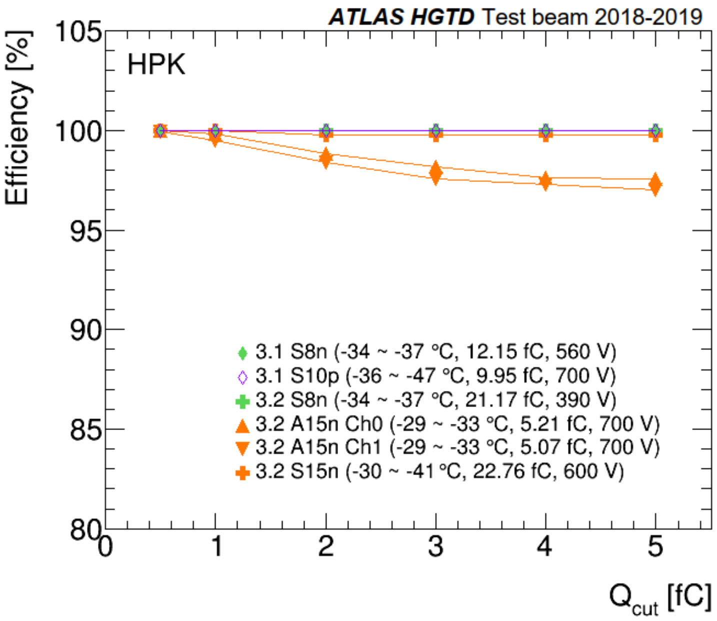

Figure 25. Efficiency as a function of the charge threshold for HPK 3.1 and 3.2 sensors.

at DESY with a 5 GeV electron beam and using a styrofoam box, filled with dry ice, which was moving upwards during data taking due to the evaporation of dry ice. The consequences of the movement/temperature variation and other different factors as the lower beam energy contribute to a more smeared plot.

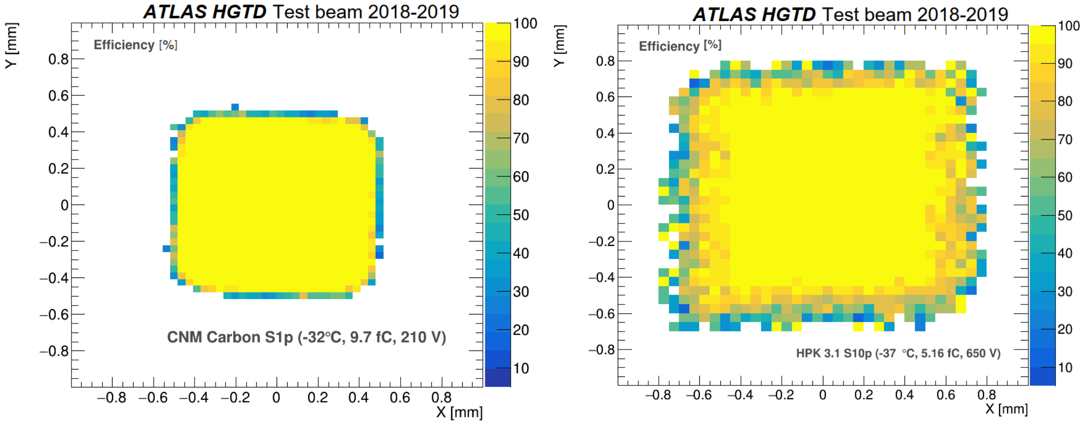

Figure 26. 2D efficiency map for CNM Carbon S1p (left) and for HPK sensor 3.1 S10n (right).

The effect of the bias voltage on the efficiency was also studied. Figures 27 and 28 show the efficiency as a function of the bias voltage for CNM and HPK sensors, respectively. In order to maintain equivalent efficiencies in highly irradiated sensors, the bias voltage has to be increased with the exception of highly irradiated CNM sensors. For the HPK sensors, 3.2 S8n has higher efficiency at lower voltages compared to 3.1 S8n since the gain for type-3.2 is higher at the same voltage, thus achieving higher efficiency earlier.

2022 JINST 17 P09026

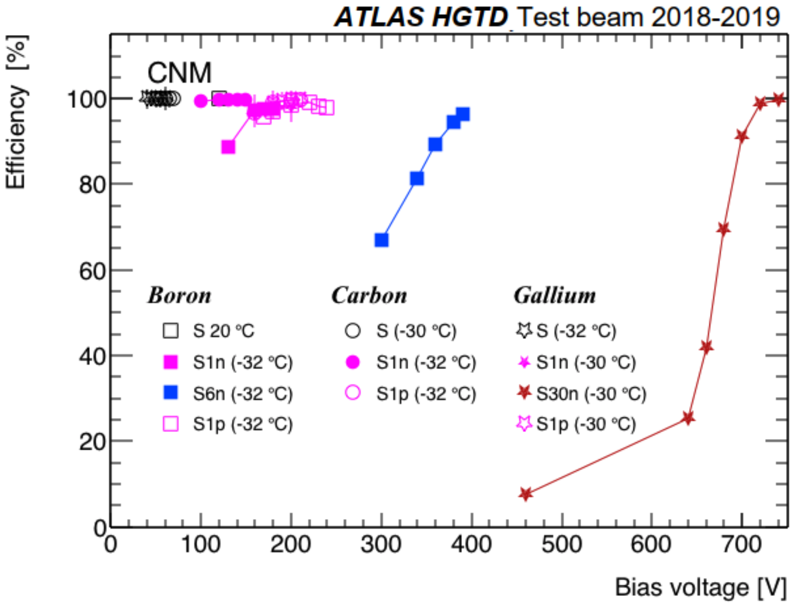

Figure 27. Efficiency as a function of the bias voltage for CNM Boron, Carbon and Gallium sensors. For each data point the charge threshold is 2 fC.

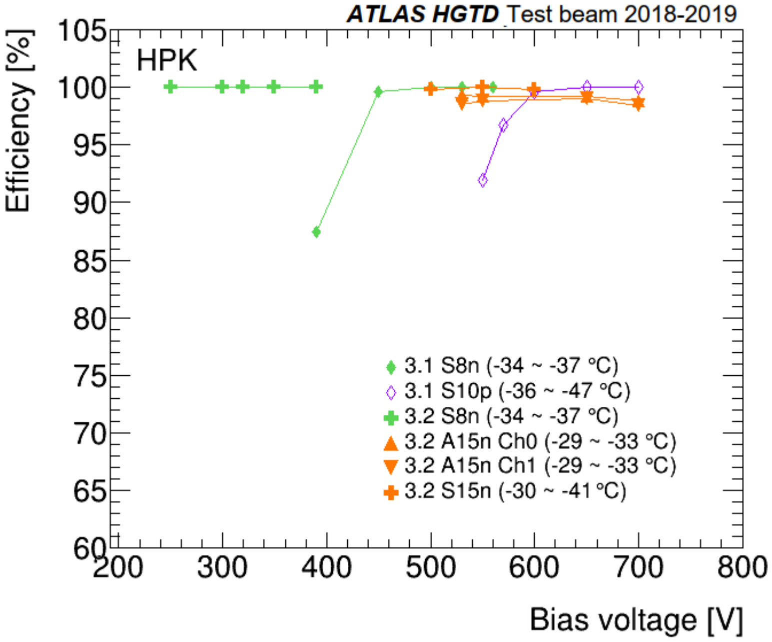

Figure 28. Efficiency as a function of the bias voltage for HPK 3.1 and 3.2 sensors. For each data point the charge threshold is 2 fC.

6 Conclusion and outlook

The ATLAS High Granularity Timing Detector will measure the time of MIPs using hybrid modules made of LGADs bump-bonded to ALTIROC chips. Before the assessment of the module performance, each component is studied separately. This paper reports the results of LGAD measurements with particle beams at CERN SPS and DESY test beam facilities. Unirradiated LGAD sensors as well as devices irradiated with neutrons or protons at different fluences were tested. Two sensor structures, single-pads and 2×2 array of pads, from two vendors, CNM and HPK, were studied. The main properties characterizing the LGADs are presented: the collected charge, the time resolution and the hit reconstruction efficiency.

In CNM LGADs, different doping materials aiming to have an improvement in radiation hardness are compared. At the same fluence, Boron plus Carbon sensors collect more charge than Boron at the same bias voltage, whereas Gallium sensors collect less charge. The addition of Carbon helps reducing the operating voltage to achieve the same amount of charge. This is extremely important at higher fluences where standard LGADs need a rather high voltage to get a good performance. The replacement of Boron by Gallium do not show clear benefits, thus this research line is not pursued. This was also confirmed by laboratory measurements.

In HPK LGADs, two different doping profiles were investigated. Type-3.2 operates at a lower voltage and performs better than type-3.1 after irradiation and it was chosen as a baseline in HGTD TDR. The worse performance before irradiation was explained by the high Boron dose.

All tested LGADs achieve the HGTD requirement of a collected charge greater than 4 fC for an ALTIROC optimal operation to perform good timing. The tested sensors reach a time resolution below 70 ps. The hit reconstruction efficiency is greater than 95% at a threshold of 2 fC for all the sensors when operated at the highest voltage point. Test beam results are in agreement with laboratory measurements. Gallium S30n meets the HGTD requirements in terms of collected charge, time resolution and hit efficiency after a fluence of 3×10^{15} $\mathrm{n_{eq}/cm^2}$.

Several beam test campaigns have been performed in 2020 and in 2021. They were devoted to study the performances of LGAD sensors from different vendors and irradiated with higher fluences up to 2.5×10^{15} $\mathrm{n_{eq}/cm^2}$ which is the radiation level expected at the end of the HL-LHC programme. These beam tests were also used to analyze the sensor mortality rates when exposed to high intensity beams to mimic end-of-life conditions of HGTD LGADs at the HL-LHC. The analysis of these measurements is ongoing. More tests are also being performed in the laboratory to understand this particular phenomenum in order to solve it in a joint effort involving both the ATLAS and CMS Collaborations as well as the different manufacturers. New productions of Carbon-enriched wafers from several vendors are also being tested. Preliminary results are very encouraging for reducing the operational point especially at high fluences.

Acknowledgments

The authors gratefully acknowledge CERN and the SPS staff for successfully operating the North Experimental Area and for continuous supports to the users. “The measurements leading to these results have been performed at the Test Beam Facility at DESY Hamburg (Germany), a member of the Helmholtz Association (HGF)”. This work was partially funded by MINECO, Spanish

Government, under grant RTI2018-094906-B-C21. This project has received funding from the European Union's Horizon 2020 research and innovation programme under the Marie Sklodowska-Curie grant agreement No. 754510. This work was partially funded by: the Spanish Government, under grant FPA2015-69260-C3-2-R and SEV-2012-0234 (Severo Ochoa excellence programme); and by the H2020 project AIDA-2020, GA no. 654168. This work was supported by the United States Department of Energy, grant DE-FG02-04ER41286.

References

[1] O. Brüning, L. Rossi, *High Luminosity Large Hadron Collider: A description for the European Strategy Preparatory Group*, Tech. Rep., CERN-ATS-2012-236 CERN, Geneva (2012).

[2] G. Apollinari et al., *High-Luminosity Large Hadron Collider (HL-LHC): Technical Design Report V.0.1*, *CERN Yellow Reports: Monographs*, CERN, Geneva (2017), http://cds.cern.ch/record/2284929.

[3] ATLAS collaboration, *Technical Proposal: A High-Granularity Timing Detector for the ATLAS Phase-II Upgrade*, Tech. Rep., CERN-LHCC-2018-023, CERN, Geneva (2018), DOI.

[4] ATLAS collaboration, *Technical Design Report: A High-Granularity Timing Detector for the ATLAS Phase-II Upgrade*, Tech. Rep., CERN-LHCC-2020-007, ATLAS-TDR-031, CERN, Geneva (2020).

[5] ATLAS collaboration, *The ATLAS Experiment at the CERN Large Hadron Collider*, 2008 *JINST* **3** S08003.

[6] ATLAS collaboration, *Technical Design Report for the ATLAS Inner Tracker Strip Detector*, Tech. Rep., CERN-LHCC-2017-005, ATLAS-TDR-025, CERN, Geneva (2017).

[7] ATLAS collaboration, *Technical Design Report for the ATLAS Inner Tracker Pixel Detector*, Tech. Rep., CERN-LHCC-2017-021, ATLAS-TDR-030, CERN, Geneva (2017), DOI.

[8] G. Pellegrini et al., *Technology developments and first measurements of Low Gain Avalanche Detectors (LGAD) for high energy physics applications*, *Nucl. Instrum. Meth. A* **765** (2014) 12.

[9] C. de La Taille, S. Callier, S.C. Di Lorenzo, N. Seguin-Moreau, P. Dinaucourt, G. Martin-Chassard et al., *ALTIROC0, a 20 pico-second time resolution ASIC for the ATLAS High Granularity Timing Detector (HGTD)*, *PoS* **TWEPP-17** (2018) 006.

[10] C. Agapopoulou et al., *Performance of a Front End prototype ASIC for picosecond precision time measurements with LGAD sensors*, 2020 *JINST* **15** P07007 [`arXiv:2002.06089`].

[11] CERN SPS North Area, http://sba.web.cern.ch/sba/BeamsAndAreas/H6/H6_presentation.html.

[12] R. Diener et al., *The DESY II Test Beam Facility*, *Nucl. Instrum. Meth. A* **922** (2019) 265 [`arXiv:1807.09328`].

[13] C. Allaire et al., *Beam test measurements of Low Gain Avalanche Detector single pads and arrays for the ATLAS High Granularity Timing Detector*, 2018 *JINST* **13** P06017 [`arXiv:1804.00622`].

[14] J. Lange et al., *Gain and time resolution of 45 μm thin Low Gain Avalanche Detectors before and after irradiation up to a fluence of* 10^{15} n_{eq}/cm^2, 2017 *JINST* **12** P05003 [`arXiv:1703.09004`].

[15] M. Carulla et al., *First 50 μm thick LGAD fabrication at CNM*, talk given at the *28th RD50 Workshop*, Torino, Italy, 2016, https://agenda.infn.it/getFile.py/access?contribId=20&sessionId=8&resId=0&materialId=slides&confId=11109.

[16] *RD50 — Radiation hard semiconductor devices for very high luminosity colliders*, http://rd50.web.cern.ch/rd50/.

[17] S. Hidalgo et al., *CNM activities on LGADs for ATLAS/CMS Timing Layers*, talk given at the *32nd RD50 Workshop*, Hamburg, Germany, 2018, https://indico.cern.ch/event/719814/contributions/3022492/.

[18] G. Kramberger et al., *Radiation hardness of thin Low Gain Avalanche Detectors*, *Nucl. Instrum. Meth. A* **891** (2018) 68 [`arXiv:1711.06003`].

[19] L. Castillo García, *A High-Granularity Timing Detector for the Phase-II upgrade of the ATLAS Calorimeter system: detector concept, description, R&D and beam test results*, 2020 *JINST* **15** C09047.

[20] H. Jansen et al., *Performance of the EUDET-type beam telescopes*, *EPJ Tech. Instrum.* **3** (2016) 7 [`arXiv:1603.09669`].

[21] O.V. Posopkina, V. Gkougkousis, and L. Castillo Garcia, *Design and integration of a SiPM based Timing Reference for ATLAS HGTD test beam*, CERN-STUDENTS-Note-2018-057, 2018.

[22] Z. Galloway et al., *Properties of HPK UFSD after neutron irradiation up to 6e15 n/cm^2*, *Nucl. Instrum. Meth. A* **940** (2019) 19 [`arXiv:1707.04961`].

[23] T. Isidori et al., *Performance of a low gain avalanche detector in a medical linac and characterisation of the beam profile*, *Phys. Med. Biol.* **66** (2021) 135002.

[24] N. Cartiglia, *Beam test studies of the LGAD sensors at FNAL*, italk given at *30th RD50 Workshop*, Krakow, Poland, 2017, https://indico.cern.ch/event/637212/contributions/2608659/.

[25] SensL TM, *C-Series datacheet: Low Noise, Blue-Sensitive Silicon Photomultipliers*, https://www.sensl.com/downloads/ds/DS-MicroCseries.pdf.

[26] D. Renker, *Geiger-mode avalanche photodiodes, history, properties and problems*, *Nucl. Instrum. Meth. A* **567** (2006) 48.

[27] SensL TM, *SMT/MLP SMA and SMTPA Board Reference Designs*, https://sensl.com/downloads/ds/TN-SMT%20Board%20Reference%20Designs.pdf.

[28] Mini-Circuits TM, *Gali-52+ Sourface Mount Monolithic Amplifier Datasheet*, https://www.minicircuits.com/pdfs/GALI-52+.pdf.

[29] U. Koetz, I. Rubinskiy, *User Manual: ATLAS FE-I4A Pixel Module as a Trigger Plane for the Beam Telescope*, https://telescopes.desy.de/images/0/08/131014_koetz-rubinsky_FEI4_as_trigger_plane.pdf.

[30] D. Cussans, *Description of the JRA1 Trigger Logic Unit (TLU), v0.2c*, Tech. Rep., EUDET-Memo-2009-4, Eudet (2009), http://www.eudet.org/e26/e28/e42441/e57298/EUDET-MEMO-2009-04.pdf.

[31] P. Ahlburg et al., *EUDAQ-a data acquisition software framework for common beam telescopes*, 2020 *JINST* **15** P01038 [`arXiv:1909.13725`].

[32] M. Backhaus, M. Barbero, L. Gonella, J. Große-Knetter, F. Hügging, H. Krüger et al., *Development of a versatile and modular test system for ATLAS hybrid pixel detectors*, *Nucl. Instrum. Meth. A* **650** (2011) 37.

[33] *LGADUtils: A C++ based framework for waveform analysis*, https://gitlab.cern.ch/egkougko/lgadutils.

[34] I. Rubinskiy, *EUTelescope. Offline track reconstruction and DUT analysis software*, Tech. Rep., EUDET-Memo-2010-12, EUDET (2010), https://www.eudet.org/e26/e28/e86887/e107460/EUDET-Memo-2010-12.pdf.

[35] *EUTelescope: A Generic Pixel Telescope Data Analysis Framework*, http://eutelescope.web.cern.ch/.

[36] L. Castillo García, E.L. Gkougkousis, C. Grieco and S. Grinstein, *Characterization of Irradiated Boron, Carbon-Enriched and Gallium Si-on-Si Wafer Low Gain Avalanche Detectors*, *Instruments* **6** (2022) 2.